

# **Generic Decoding of Seen and Imagined Objects using Hierarchical Visual Features**

## **Authors:**

Tomoyasu Horikawa<sup>1</sup> and Yukiyasu Kamitani<sup>1,2\*</sup>

## **Affiliations:**

<sup>1</sup>ATR Computational Neuroscience Laboratories, Kyoto 619-0288, Japan

<sup>2</sup>Graduate School of Informatics, Kyoto University, Yoshida-honmachi, Sakyo-ku, Kyoto 606-8501, Japan

\*Corresponding author's email address: kamitani@i.kyoto-u.ac.jp

# Abstract

Object recognition is a key function in both human and machine vision. While recent studies have achieved fMRI decoding of seen and imagined contents, the prediction is limited to training examples. We present a decoding approach for arbitrary objects, using the machine vision principle that an object category is represented by a set of features rendered invariant through hierarchical processing. We show that visual features including those from a convolutional neural network can be predicted from fMRI patterns and that greater accuracy is achieved for low/high-level features with lower/higher-level visual areas, respectively. Predicted features are used to identify the target object (extending beyond decoder training) from a set of computed features for numerous objects. Furthermore, we demonstrate the identification of imagined objects, suggesting the recruitment of intermediate image representations in top-down processing. Our results demonstrate a tight link between human and machine vision and its utility for brain-based information retrieval.

# Introduction

Brain decoding through neuroimaging analysis of functional magnetic resonance imaging (fMRI) activity patterns has enabled the interpretation of mental contents, including what people see<sup>1,2</sup>, maintain in working memory<sup>3-5</sup>, imagine<sup>6-9</sup>, and dream<sup>10</sup>. Most of the studies relied on a classification-based approach, where a statistical classifier (decoder) is trained to learn a relationship between brain activity patterns and the target contents to be decoded. Such an approach, however, entails a fundamental constraint on the number of possible outputs. Namely, the outputs are limited to the number of classes used for decoder training, preventing the decoder from making predictions about any classes that are not used in training.

Recent studies have overcome the limitation on the number of possible outputs by designing decoders for retinotopically organized, image-level features<sup>11-13</sup>. This enabled the decoding of novel visual images that were not presented during training sessions, thereby identifying images that are similar to the images viewed by subjects<sup>11,12</sup>, and reconstructing viewed visual images from measured brain activity patterns<sup>13</sup>. Kay et al. (2008)<sup>11</sup> built an encoding model consisting of retinotopically organized Gabor wavelet filters. They used a database of visual images and the predicted brain activities produced by an encoding model. The measured brain activity was then decoded by determining the visual image in the database corresponding to the predicted brain activity most similar to the measured brain activity. It was also demonstrated that this technique can be used to identify remembered works of art from brain activity patterns in the early visual areas<sup>14</sup>. Miyawaki et al. (2008)<sup>13</sup> constructed a modular decoding model consisting of multi-scale local decoders (modules) that predicted the contrast of local image patches of various scales. The model was able to reconstruct arbitrary visual images from measured brain activity by combining the outputs

of the local decoders despite having been trained with brain activities measured for a small number of random images.

While the image identification<sup>11,12,14</sup> and visual image reconstruction<sup>13</sup> approaches are suitable for decoding according to image-based similarity, they do not provide explicit information regarding the object a person is seeing or imagining. The possible objects that we may see or imagine in daily life are countless, and object-based information is often of more direct relevance to our visually guided behavior than image-based information. Establishing a method to decode generic object categories from brain activity would provide practical benefits for technologies utilizing information decoded from brain activity, and may enrich our understanding of how the human brain represents a vast number of objects.

In the present study, we aim to decode seen and imagined object categories, including those that were not used in decoder training, from fMRI signals measured while subjects either viewed or imagined object images. We extend the modular decoding approach originally developed for visual image reconstruction<sup>13</sup> to the decoding of generic object categories.

To tailor the modular decoding approach to our objectives, we assumed that an object category can be represented by a set of visual features with several invariances. These features correspond to those proposed for the object recognition challenge in machine vision<sup>15-21</sup> (Fig. 1a), which aims at enabling a computer to recognize objects in images according to their category names. The selection of the visual features is a critical aspect of this approach because even if images depict the same object, they do not necessarily have pixel-wise similarity as a result of varying rotation, scale, position, and other attributes. Thus, objects may be more suitably represented using mid- or high-level visual features which are invariant to such image differences rather than the low-level features (e.g., local

contrast<sup>13</sup> or Gabor wavelet filter<sup>11,12,14</sup>) used for visual image reconstruction and image identification.

We tested a total of 13 candidates of visual feature types/layers constructed from four models (Fig. 1a, see Methods): a convolutional neural network (CNN) model<sup>17</sup> (CNN1-CNN8), HMAX model<sup>18-20</sup> (HMAX1-HMAX3), GIST<sup>21</sup>, and scale invariant feature transform<sup>15</sup> combined with "Bag of Features"<sup>16</sup> (SIFT+BoF). It has been reported that representations of these model outputs are statistically similar to visual cortical activity<sup>18,19,22-27</sup>.

Using these visual features, we present an approach called *generic object decoding* in which arbitrary object categories are decoded from human brain activity (Fig. 1b). We used the online image database, *ImageNet*<sup>28</sup> and trained regression models (decoders) to predict visual features extracted by the computational models from brain activities recorded by fMRI while subjects viewed natural images (150 categories). The trained decoders were then used to predict feature vectors of seen and imagined objects that were not used in decoder training from the fMRI activity patterns. By comparing the predicted feature vector with the object feature vectors calculated from images in the image database, we identify seen and imagined objects from object categories defined in the database (15,372 categories). Note that because arbitrary object categories are represented in this feature space, the identified object categories are not limited to those used in the training session.

Here, we first demonstrate that visual feature values of seen objects calculated by the computational models can be predicted from multiple brain areas, showing tight associations between hierarchical visual cortical areas and the complexity levels of visual features. We also show that the stimulus-trained decoders can be used to decode visual features of imagined objects, providing evidence for the recruitment of feature-level

representations in top-down visual imagery. Finally, we test whether the features predicted from brain activity patterns are useful for identifying seen and imagined objects for arbitrary categories.

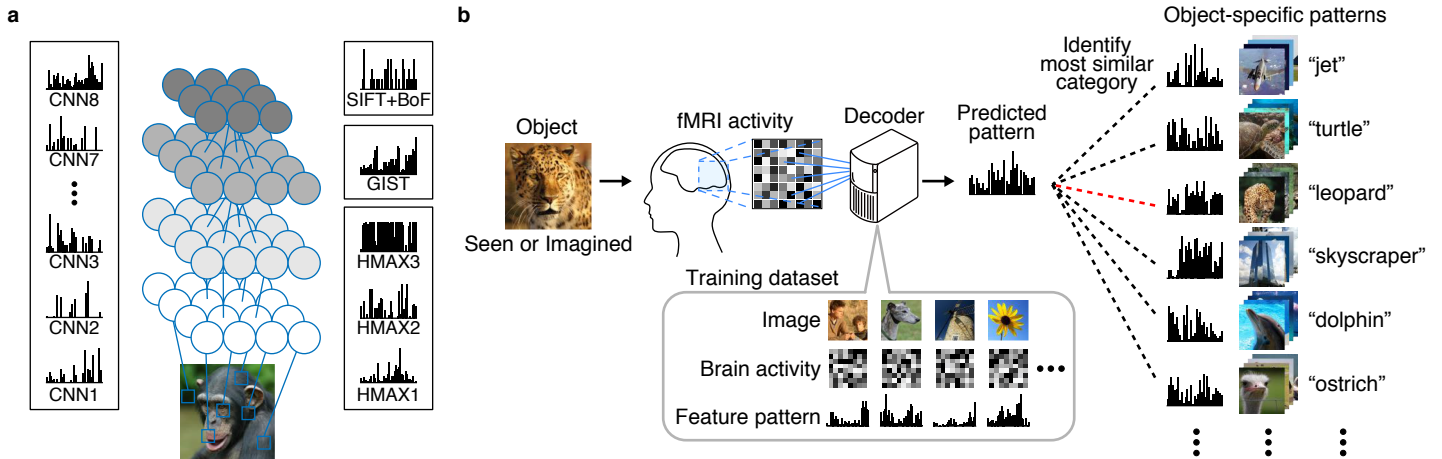


**Figure 1 | Generic object decoding.** (a) Visual feature extraction from natural images using computational models. Visual features are calculated from natural images using CNN (CNN1–8), HMAX (HMAX1–3), GIST, and SIFT+BoF (see Methods for details). (b) Overview of generic object decoding. fMRI activity was measured while subjects viewed natural images. Decoders are trained to predict the values of the visual features for presented images/objects from multi-voxel fMRI signals. Given measured fMRI activity, a feature vector is predicted and it is used to identify the seen or imagined object by comparing it with the feature vectors of numerous objects in an annotated image database including those not used for decoder training.

# Results

## Generic object decoding

Our objective was to decode arbitrary object categories (which were not included in model training) from human brain activity measured using fMRI. Our approach consisted of the following steps. First, we extracted feature values from object images using a total of 13 types/layers of visual features (CNN1–8, HMAX1–3, GIST, and SIFT+BoF; ~ 1,000 feature units for each feature type/layer). We thereby represented an object image by a feature vector of each feature type/layer (Fig. 1a). Second, decoders were trained to predict the vectors of visual features of seen objects from brain activity patterns (Fig. 1b). Third, using the trained decoders, a feature vector was predicted from brain activity measured while seeing or imagining an object, which was not used in decoder training. Finally, the predicted feature vector was used to identify a seen or imagined object by calculating the similarity between the predicted feature vector and the object feature vectors calculated from an annotated image database.

To represent an object image by a feature vector, we used four types of computational models with 13 visual feature types/layers. Some of the models emulate the structure of hierarchical human visual system (CNN and HMAX), and the others are models designed for object or scene recognition in machine vision (GIST and SIFT+BoF).

The CNN model is an artificial neural network with a deep hierarchical structure consisting of five convolutional layers (CNN1–5) and three fully-connected layers (CNN6–8). It is trained to discriminate object categories in a supervised manner. CNN models have demonstrated high object discriminability for the generic object recognition challenge<sup>17</sup>, and the features in each CNN layer were found to represent visual image properties similarly to each brain area in the visual hierarchy<sup>22-25</sup>.



The HMAX model is also a hierarchical model that extends the simple and complex cells of Hubel and Wiesel<sup>29,30</sup> to emulate the biological processing involved in object recognition. We used a version of the HMAX model that consists of three layers of simple and complex processing stages<sup>19</sup> (HMAX1–3).

GIST is a model developed for the computer-aided scene categorization task<sup>21</sup>. The GIST descriptor computes coarsely localized spectral information and captures global low-level image properties.

Features obtained from SIFT with BoF (SIFT+BoF) emulate the functional properties of human visual object recognition, and are invariant to image scaling, translation, and rotation. They are partially invariant to illumination changes and affine or 3D projection. Using a pattern of luminance gradient calculated from a local patch on images, object images are parameterized by the frequency of similar patterns in each image.

To test the feasibility of generic decoding of seen and imagined objects from human brain activities, we conducted two fMRI experiments: an image presentation experiment, and an imagery experiment (Fig. 2). In the image presentation experiment, fMRI signals were measured while subjects viewed a sequence of visual object images, each presented for nine seconds (Fig. 2a). The image presentation experiment consisted of two sessions: the training image session and the test image session. In the training image session, a total of 1,200 images from 150 different object categories (eight images from each category) were each presented once. In the test image session, a total of 50 images from 50 object categories (one image from each category) were each presented 35 times. In the imagery experiment, fMRI signals were measured while the subjects imagined about one of the 50 object categories (10 times for each category) that were presented in the test image session of the image presentation experiment (Fig. 2b). Note that the categories in the test image

session and the imagery experiment were not used in the training image session. While we show results with fMRI signals averaged across all trials (35 trials for the test image session in the image presentation experiment, and 10 trials for the imagery experiment), quantitatively similar results were obtained with a much smaller number of averaged samples (see Supplementary Information).

We performed our analysis for each combination of feature types/layers (CNN, HMAX, GIST, and SIFT+BoF) and brain regions of interest (V1, V2, V3, V4, the lateral occipital complex [LOC], fusiform face area [FFA], parahippocampal place area [PPA], and an entire visual cortex covering all of the visual subareas listed above [visual cortex, VC]).

A set of linear regression functions (sparse linear regression model<sup>31</sup>) was used to predict visual feature vectors (~1,000 feature units for each feature type/layer; see Methods) from the fMRI signals corresponding to each brain area. A unit decoder was trained to predict the values of a unit of the feature vectors calculated from the viewed objects, using the fMRI signals from the training image session. The trained decoders were then used to predict the vectors of each feature type/layer for test object categories from measured fMRI signals in the test image session and the imagery experiment.

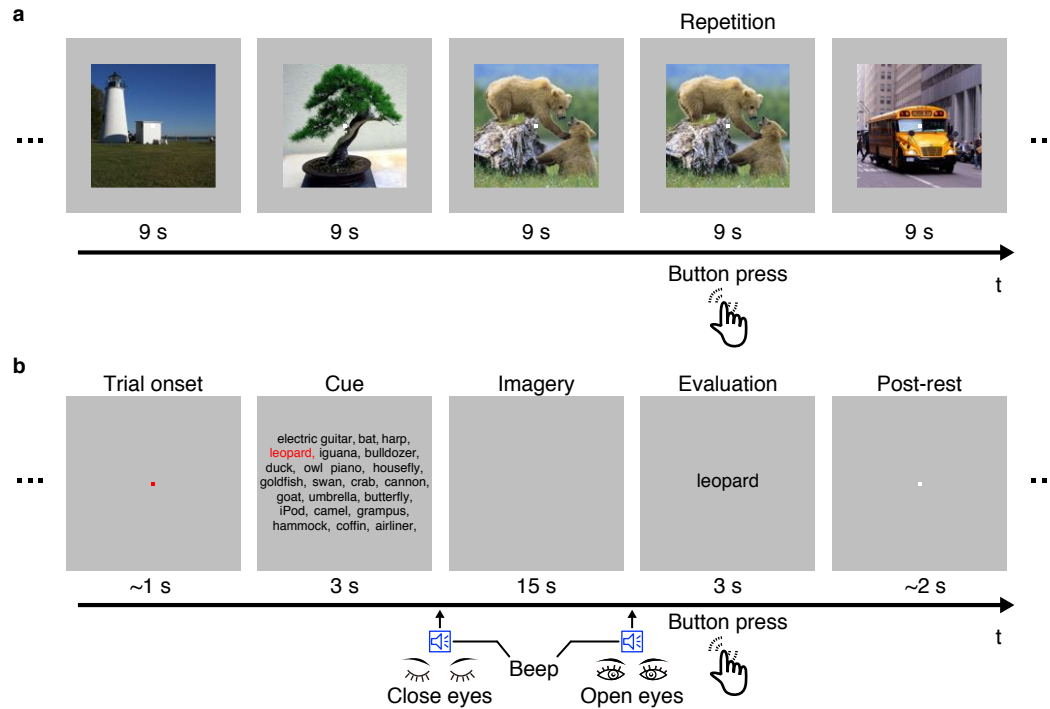


**Figure 2 | Experimental design.** (a) Image presentation experiment. Images were presented in the center of the display with a central fixation spot. The color of the fixation spot changed from white to red for 0.5 seconds before each stimulus block started to indicate the onset of the block. Subjects maintained steady fixation throughout each run and performed a one-back repetition detection task on the images, responding with a button press for each repetition. (b) Imagery experiment. The onset of each trial was marked by a change in the fixation color. Cue stimuli composed of an array of object names were visually presented for 3 seconds. The onset and the end of the imagery periods were signaled by aural beeps. After the first beep, the subjects were required to imagine as many object images as possible pertaining to the category indicated by red letters. They continued imagining with their eyes closed (15 seconds) pending a second beep. Subjects were then asked to evaluate the vividness of their mental imagery (3 seconds). Note that the actual cue consisted of an array of 50 object names, while only subsets of the words are depicted in this figure because of space limitation.

## Image feature decoding

We first investigated whether we could decode the values of visual feature vectors for presented images from brain activity patterns in multiple brain areas. Decoding performance was evaluated by the correlation coefficient between true and predicted feature values of each feature unit (Fig. 3a). Correlation coefficients were averaged across the units in each feature type/layer for multiple brain areas, and then pooled across five subjects. Because the distribution of feature values and the number of feature units of the original population differed between feature types/layers, interpreting decoding accuracy differences across feature types/layers is difficult. For example, when the accuracy was evaluated by normalized root mean square errors, the overall pattern of performance across feature types/layers was different from that of correlation (Supplementary Fig. 1). Therefore, in the following we mainly focused on the pattern of accuracies across brain regions in each feature type/layer.

Figure 3b shows the decoding accuracy for features of presented images in multiple brain areas. The feature values predicted from brain activity positively correlated with the true values for all feature–ROI combinations ( $t$  test, uncorrected  $p < 0.05$ ). Interestingly, the choice of feature types/layers and brain areas affected the pattern of accuracy. As clearly observed in the results corresponding to the CNN features, higher-order visual features tended to be better predicted from fMRI signals in higher rather than lower cortical areas, and lower-order visual features tended to be better predicted from fMRI signals in lower rather than higher cortical areas. Similar tendencies were also observed in the HMAX model and the other two models. These results reveal a tight association between hierarchical visual areas and the complexity levels of visual features in image feature decoding accuracy.

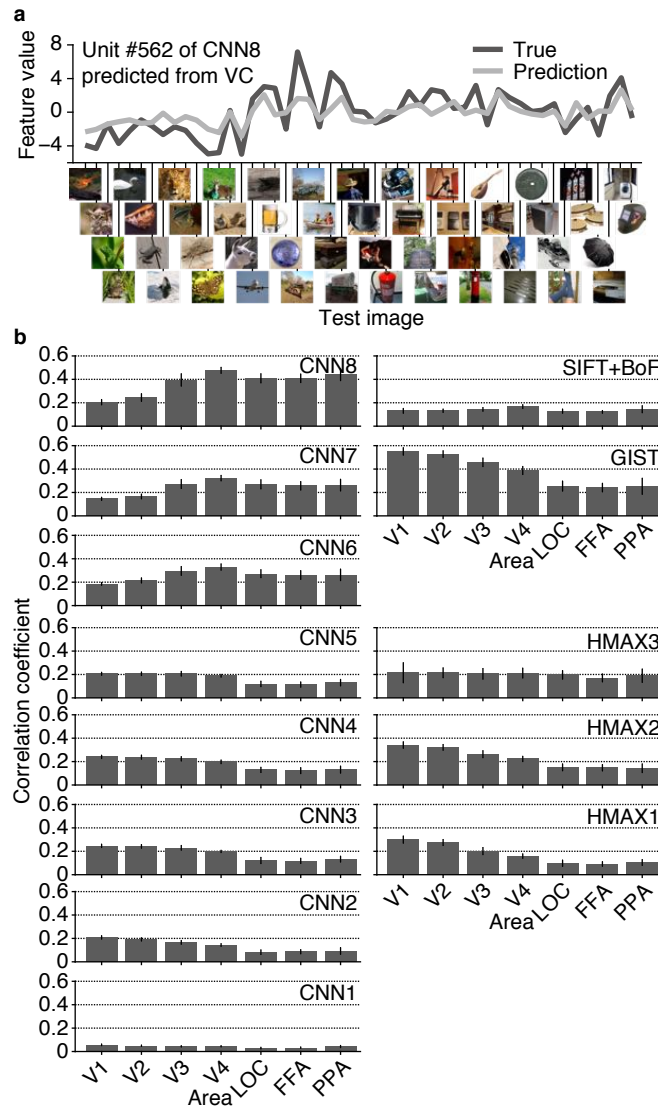


**Figure 3 | Image feature decoding.** (a) Example of a feature unit. True (black) and predicted (light gray) feature values for 50 test images are shown for Unit #562 of CNN Layer 8 (CNN8) predicted from the whole visual cortex (VC). (b) Image feature decoding accuracies. Mean decoding accuracies are shown for each feature type (layer) and brain area (error bars, 95% confidence interval (CI) across five subjects).

## Object feature decoding

To adjust the decoding models to decode features of imagined object categories, we customized the decoders to predict representative feature vectors of individual object categories from fMRI signals. This is because we let the subjects freely imagine visual images of specified object categories in the imagery experiment, and there were no ground truth images for their imagination. For that reason, we trained the decoders again by using object feature vectors, constructed by averaging the feature vectors of multiple images annotated with individual object categories. We then tested whether the decoder could predict object feature vectors of the categories seen or imagined by the subjects.

The prediction accuracy for object features of seen and imagined object categories in multiple brain areas is shown in Fig. 4 (see Supplementary Fig. 2 for distributions of prediction accuracy for individual feature units averaged across subjects). The trained decoders successfully predicted the object feature vectors of the seen categories for all feature–ROI combinations (Fig. 4a;  $t$  test, uncorrected  $p < 0.05$ ). In contrast to the performance trend in the image feature decoding analysis (Fig. 3b), the object feature vectors were better predicted from fMRI signals in higher than in lower cortical areas for most of the visual features. Furthermore, the object feature vectors of imagined object categories were also suitably predicted for most of the features using the same decoders trained on relatively higher visual cortical activities (V4, LOC, FFA, and PPA), while the decoders trained on the lower visual cortical activities (V1 and V2) showed the accuracy close to the chance (Fig. 4b). These results suggest that decoders trained to predict feature vectors of seen objects can generalize to predict the feature vectors of imagined object in relatively higher visual cortices. This provides evidence that imagining about an object category induces brain activity associated with elemental visual features.

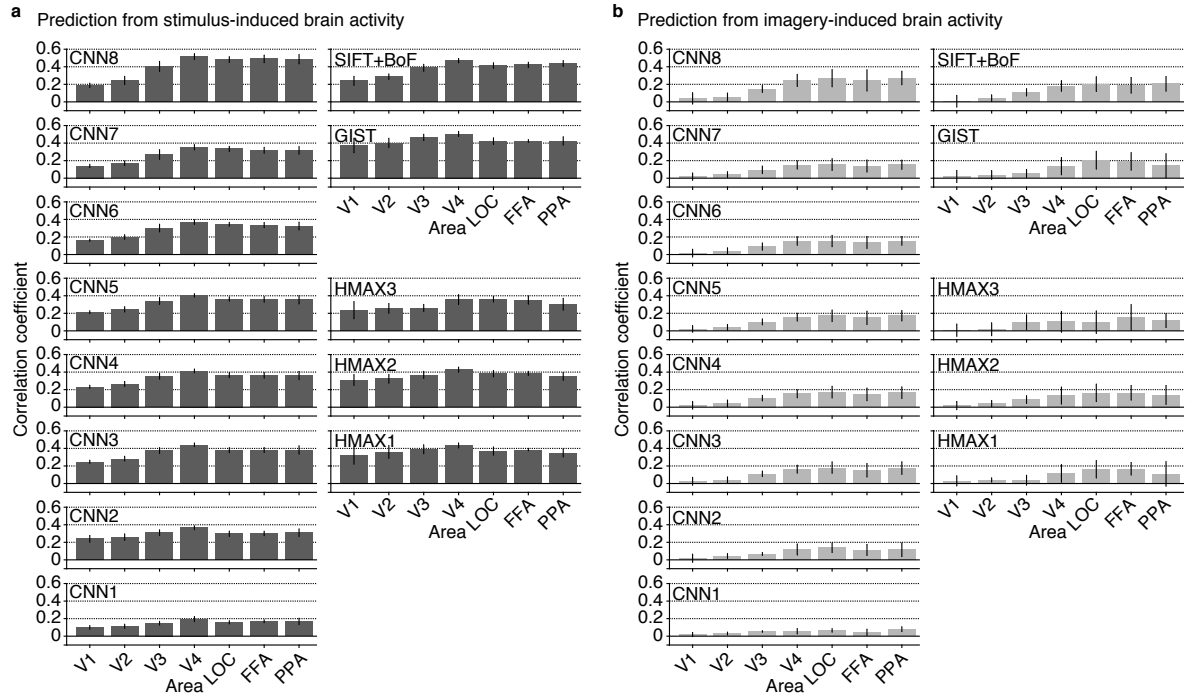


**Figure 4 | Object feature decoding.** (a) Accuracies obtained by predicting features from stimulus-induced brain activity. (b) Accuracies obtained by predicting features from imagery-induced brain activity. Mean decoding accuracies are shown for each feature type (layer) and brain area (error bars, 95% CI across five subjects).

Additionally, we found that the object feature decoding accuracy in each unit was positively correlated with the “category discriminability” of each unit (Fig. 5). As an index of category discriminability, we calculated the  $F$  statistic of each feature unit (a ratio of inter- and intra-category variations of feature values calculated from images in the *ImageNet* [15,322 categories]). The distributions of the category discriminability from each feature type/layer showed that the high-level visual features tend to demonstrate high discriminability for both the HMAX and CNN models (Fig. 5a bottom). Within each feature type/layer, positive correlations between decoding accuracy and category discriminability were observed for all visual features except for the HMAX1 (Fig. 5b and c). Furthermore, decoding accuracy and category discriminability were positively correlated even when feature units were combined across all feature types/layers (Fig. 5c, All;  $r = 0.38$ , 95% CI across five subjects [0.35, 0.41]) and when feature units were averaged within each feature type/layer (Fig. 5c, Mean;  $r = 0.59$ , 95% CI across five subjects [0.55, 0.63]) (Fig. 5a top, and c). While this analysis was performed with decoders trained on the whole visual cortical activity (VC), the similar tendency was robustly reproduced with decoders trained on brain activity from each visual subarea. Thus, decodable visual feature units tend to be critical for defining object categories.



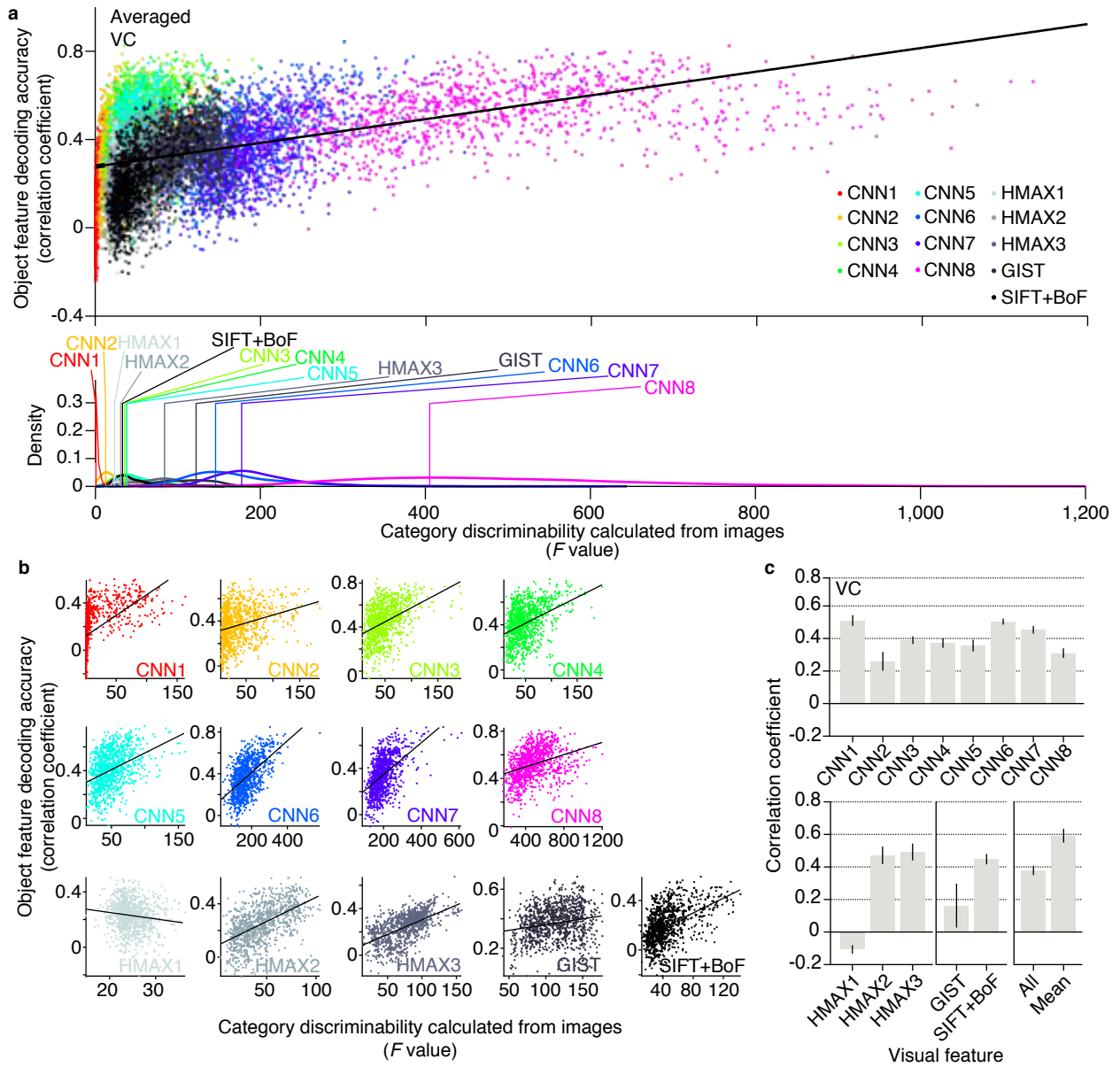


**Figure 5 | Category discriminability versus decodability of individual feature units. (a)**

Scatterplot of object feature decoding accuracy against category discriminability for all the feature types/layers (top panel, predicted from VC, average over five subjects for each unit) and distributions of the category discriminability for each feature type/layer (bottom panel; vertical lines denote the mode of each distribution). Each dot in the scatter plot denotes the  $F$  statistic and decoding accuracy

for a feature unit ( $\sim 1,000$  units). The solid line indicates a fitted regression line. **(b)** Scatterplots for individual feature types/layers. **(c)** Correlation coefficients between category discriminability and object feature decoding accuracy (error bars, 95% CI across five subjects).

## Object category identification

We conducted identification analysis<sup>11,13</sup> to examine whether a feature vector predicted from brain activity is useful for identifying the seen or imagined object. Because our approach is not constrained by the number of categories used in the training of the decoding model, we can perform identification analysis for thousands of object categories, including those not used for model training. Here, the category of the seen or imagined object was identified from a variable number of candidate categories (Fig. 6). We constructed the candidate feature vector set consisting of object categories used in the test image session (and the imagery experiments) and a specified number of object categories randomly selected from the 15,322 categories provided by *ImageNet*<sup>28</sup>. Given an fMRI sample, category identification was performed by selecting the object feature vector with the highest correlation coefficient with the predicted feature vector.

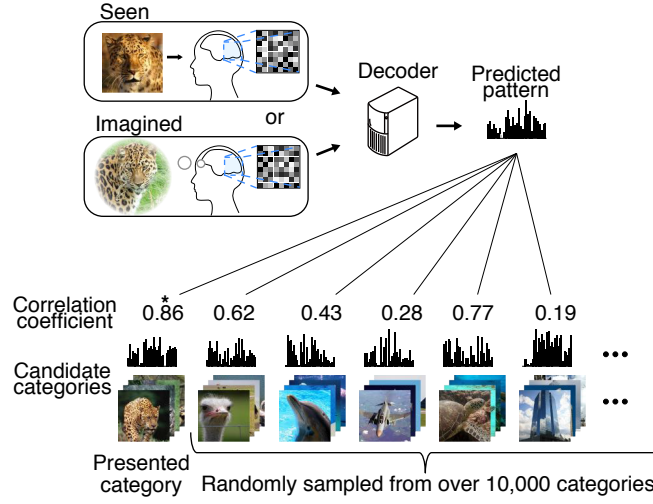


**Figure 6 | Category identification procedure.** The correlation coefficient was calculated between a predicted feature vector and the object feature vectors for categories in the candidate set, consisting of the presented or imagined category and a specified number of categories randomly selected from the *ImageNet* database<sup>28</sup>. The category with the highest correlation coefficient was selected as the predicted category (marked by a star).

First, we illustrate examples with the top six categories selected from 1,000 candidates (Fig. 7a; CNN8; predicted from VC; candidate sets consisting of each one of the true categories [ $n = 50$ ] and 999 randomly selected false categories). For both seen and imagined objects, the true object categories were correctly selected or highly ranked. Even when the correct categories were not assigned, the top six categories appeared to include similar or related categories (e.g., in Fig. 7a, the decoded feature vector for “duck” misidentified another type of bird “rock wren”).

Next, we quantitatively evaluated the relations between rank and semantic distance with respect to the target object categories and the categories ranked in each position. We

defined the semantic distance by the shortest path length between the categories in the *WordNet* tree<sup>32</sup>, and the semantic distance was calculated between the target category and each of the 1,000 candidate categories. The 1,000 distances were then sorted by the object category ranking (the similarity to the decoded feature vector), and averaged over 1,000 repetitions of random candidate selection and 50 target categories. The analysis showed that the categories ranked in higher positions tended to show shorter semantic distance to the target categories (Fig. 7b). The semantic distance was positively correlated with rank, especially for the higher-level CNN features and SIFT+BoF (Fig. 7c). This was true under both seen and imagined conditions. These results suggest that for these feature types/layers, semantically similar, if not correct, categories can be selected with the feature vector predicted from brain activity.

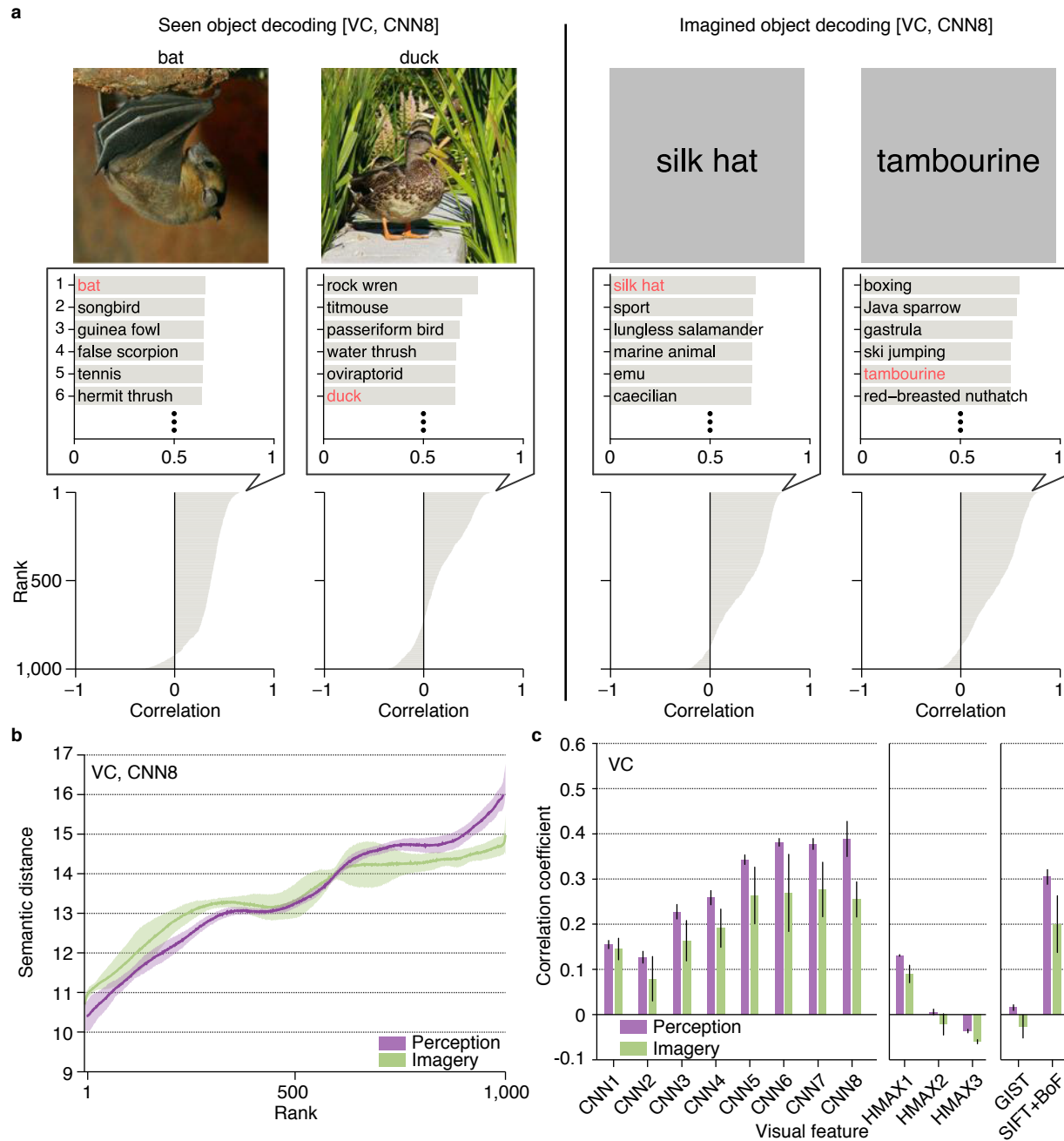


**Figure 7 | Object categories ranked by the similarity to decoded feature vectors. (a)** Rankings of object categories are shown for two viewed objects (“bat” and “duck”, top panel) and two imagined objects (“silk hat” and “tambourine”, top panel), calculated with the CNN8 feature vectors predicted

from the VC activity. The candidate object names and correlation scores for the top six objects with the highest correlation coefficients are shown in the middle panels (correct object names indicated in red). The panels at the bottom illustrate the correlation coefficients for 1,000 object categories in descending order. **(b)** Relationship between the object category ranking and the semantic distance (CNN8 predicted from VC). Shaded areas denote 95% CI across five subjects. **(c)** Correlation coefficients between the rank and the semantic distance for all feature types/layers (predicted from VC). Correlation coefficients were calculated for each candidate set and target category, and then averaged across 1,000 repetitions of candidate selection and 50 target categories (error bars, 95% CI across five subjects).

Finally, for quantitative evaluation, we assessed the identification performance of seen and imagined objects when the number of candidate sets was two (Fig. 8, predicted from VC, chance level = 50%, see Supplementary Fig. 3 for identification accuracy as a function of the number of average samples). The analysis revealed that both seen and imagined objects were successfully identified at a statistically significant level with all feature types/layers ( $t$  test, uncorrected  $p < 0.05$ ). Furthermore, when the same identification analysis was performed for each ROI, above-chance performance was achieved for most of the feature–ROI combinations (Supplementary Fig. 4). Intriguingly, mid-level features decoded from higher cortical areas were the most useful in identifying both seen and imagined object categories.



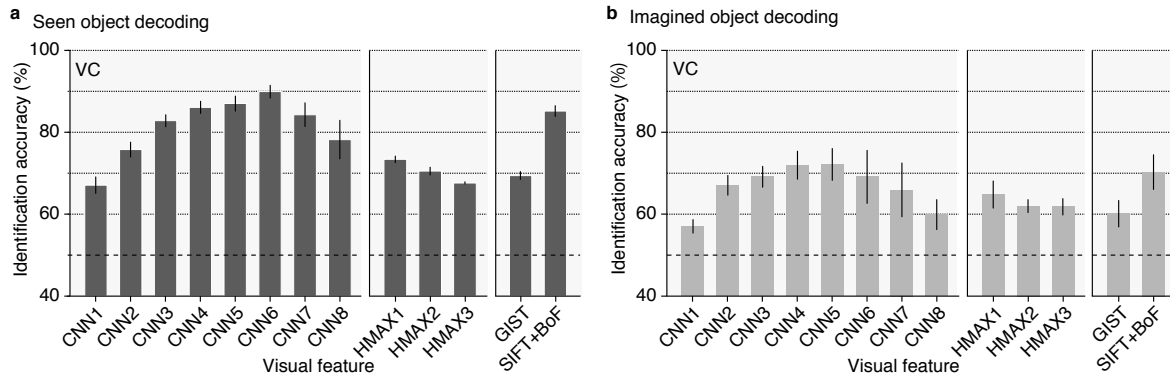


**Figure 8 | Identification performance.** Identification was performed for all combinations of one of the 50 test object categories and one of the 15,322 candidate categories (identification from two categories; error bars, 95% CI across five subjects; dashed line, chance level, 50%). **(a)** Seen object identification performance. **(b)** Imagined object identification performance. While this identification analysis was performed with the decoders trained to predict object feature vectors (used for the results of Fig. 4), the decoders trained to predict image features of presented images (the image feature decoders used for the results of Fig. 3) can also be used. See Supplementary Fig. 5 and 6 for the identification performance obtained by the image feature decoders.

## Discussion

We have shown that arbitrary object categories seen and imagined by subjects can be predicted from fMRI signals of the human visual cortex. The trained decoders successfully predicted the individual feature values of the presented images. Higher-order and lower-order visual features tended to be better predicted from fMRI signals in higher and lower cortical areas, respectively. Further, stimulus-trained decoders can be used to predict the feature vector of both seen and imagined objects, enabling the identification of seen and imagined objects from fMRI signals. This was achieved despite not using the same categories for decoder model training. Interestingly, mid-level features were the most useful in identifying object categories, suggesting the significant contributions of mid-level representations in accurate object identification. Our results demonstrate that the decoding model trained on a limited set of object categories generalizes to decode arbitrary object categories, providing a proof of concept for generic object decoding. Moreover, successful object category identification for imagery-induced brain activity suggests that feature-level representations elicited in visual perception may also be used for top-down visual imagery.

Our analyses demonstrated that visual features extracted by computational models were successfully predicted from brain activity patterns (Fig. 3). The analysis revealed a close association between the cortical hierarchy and the levels of visual feature representations. These results were consistent with the previous studies that investigated the representational similarities between brain activity and SIFT+BoF<sup>27</sup> and CNN model<sup>24</sup>, and those that used visual features of a hierarchical neural network to predict neural responses to visual images<sup>22,23,25</sup>. These studies showed a high representational similarity between the top layer of a convolutional neural network and visual cortical activity in the inferior temporal (IT) cortex of humans<sup>24,25</sup> and non-human primates<sup>22,23</sup>. Moreover, Cadieu et al.

(2014)<sup>22</sup> and Yamins et al. (2014)<sup>23</sup> both reported that the features from the middle layer of a hierarchical neural network can accurately predict V4 brain activity. In addition, Güçlü and van Gerven (2014)<sup>25</sup> revealed an explicit gradient for the feature complexity in the visual cortical hierarchy using the encoding approach. Our results complement these findings by revealing the correspondence in individual subareas in both the lower and higher visual cortex using the decoding approach. We thus support further for the theory that a CNN can be a good proxy for the hierarchically structured feed-forward visual system for object recognition.

In our analyses, we selected 1,000 feature units to reduce the computational cost, as some layers of the CNN model (CNN1–7) originally had more than 100,000 features. It may have been possible that the selection of the 1,000 feature units biased the results. To verify that this was not the case, we repeated the same identification analysis by resampling feature units from the original feature populations and changing the number of feature units from 10 to 1,000 repeatedly (10 times resampling; Supplementary Fig.7). The additional analysis demonstrated that the identification accuracies of most visual feature types/layers were almost saturated when several hundreds of feature units were used, and qualitatively similar results to our main results were obtained for different numbers of feature units.

Our results may be relevant to the long-standing debate as to whether mental imagery is symbolic (language-like) or depictive (picture-like)<sup>33,34</sup>. They provide novel evidence that intermediate feature-level representations between symbolic and depictive representation may also emerge during mental imagery. The decoder trained on brain activity induced by visual stimuli was able to predict the feature vector of not only seen but also imagined objects, especially when relatively higher visual areas were used (Fig. 4). This enabled the identification of imagined objects using the feature vector decoded from brain activity during imagery (Fig. 8b). These results show that the stimulus-trained decoders could

generalize to the imagery condition. Several previous studies have shown that the same neural representations are used during perception and mental imagery for low-level image properties<sup>3-5,14</sup> and high-level semantic representations<sup>6-9</sup>, depending on the tasks performed by subjects. In contrast, our results indicate that intermediate feature-level representations were also recruited during top-down mental object imagery.

By extending the modular decoding approach previously proposed in our visual image reconstruction study<sup>13</sup> to high-level vision, we were able to decode visual object categories even if the predicted objects were not included in the training dataset (Fig. 7 and 8). Since images depicting the same kinds of objects do not necessarily have pixel-wise similarity, complex and invariant features appear to be suitable for object identification. However, a simulation study suggests that intermediate-level rather than overly complicated visual features are better for object discrimination<sup>35</sup>. Our additional analysis with true feature vectors calculated from stimulus images (with no prediction errors; equivalent to generic object recognition in machine vision) also showed a slightly poorer identification with CNN8 than with CNN7 (Supplementary Fig. 8). Consistent with these observations, our results from decoded feature vectors showed the highest identification accuracy with mid-level features rather than higher-level features. The results suggest the suitability of mid-level features for object representation, possibly consistent with electrophysiological studies of the monkey inferior temporal cortex<sup>36,37</sup>.

In the present study, we used a decoding approach to link neural activity and visual features. In contrast, other studies used representational similarity analysis (RSA)<sup>24,38-41</sup> or encoding approaches<sup>11,12,14,22,23,25</sup>. While the RSA and encoding approaches can evaluate mass characteristics of each visual feature type/layer (e.g., a specific layer of a convolutional neural network) associated with brain activity, our decoding approach can characterize individual feature unit in terms of the decodability from distributed brain activity patterns.

As Khaligh-Razavi et al. (2014)<sup>24</sup> demonstrated, computational models with a high representational similarity to activity patterns in the inferior temporal cortex showed better categorization accuracy. Thus, it may be possible to use the prediction accuracy of individual feature units as a guide to find effective feature units for better object recognition performance in machine vision. Indeed, our analysis revealed that the feature units better predicted from brain activity patterns showed high category discriminability (Fig. 5). This finding is consistent with the conclusions of previous studies<sup>22-24</sup>, and supports the notion that feature decoding accuracy may be a suitable guide for selecting better features for object recognition.

Our identification analyses revealed that highly ranked candidate categories tended to be semantically similar to the target categories for most of the CNN features and SIFT+BoF (Fig. 7b and c). Therefore, even when the final identification was incorrect, we were able to predict categories that were semantically similar to the target category. However, such a tendency was not observed with the HMAX and GIST. Because the GIST captures low-level image properties<sup>21,26</sup>, it is not surprising that rank and the semantic distance were not correlated for this feature. On the other hand, the HMAX model was designed to model the higher-level visual system, but did not show positive correlations between rank and semantic distance. This may suggest that the feature vectors of the HMAX model cannot capture the semantics of objects, which is consistent to the indications of several previous studies<sup>24,38-41</sup>.

Our approach allows the decoding of arbitrary objects not limited to those used to train the decoder in advance. This is a significant scientific and practical contribution, especially in situations where it is unknown what kind of objects should be decoded. For example, because our approach can decode objects from mental imagery, we may be able to apply our method to decode the contents of dreaming or daydreaming<sup>10</sup>. Reading contents of such

spontaneously generated thinking would be greatly beneficial in understanding the functions of such cognitive phenomena. Achieving this requires distinguishing the conceivable differences in neural representation between volitional mental imagery and spontaneous mental imagery. This formulates a challenging problem in future work. In addition, our approach may provide a basis for a brain-based information retrieval system by translating brain activity into words or concepts. Using the outputs of decoding models, our approach may create a query for an information retrieval system based on brain activity.

# Methods

## Subjects

Five healthy subjects (one female and four males, aged between 23 and 38) with normal or corrected-to-normal vision participated in the experiments. All subjects provided written informed consent for their participation in the experiments, and the study protocol was approved by the Ethics Committee of ATR.

## Visual images

Images were collected from the online image database *ImageNet*<sup>28</sup> (<http://www.image-net.org/>; 2011 fall release), an image database where images are grouped according to the hierarchy in *WordNet*<sup>32</sup>. We selected two hundred representative object categories (synsets) for stimuli in the visual image presentation experiment. After excluding images with a width or height less than 100 pixels or aspect ratio over 1.5 or under 2/3, all of the remaining images in *ImageNet* were cropped to the center.

## Experimental design

We conducted two types of experiments: an image presentation experiment, and an imagery experiment. All visual stimuli were rear-projected onto a screen in an fMRI scanner bore using a luminance-calibrated LCD projector.

The image presentation experiment consisted of two distinct sessions: a training image session and a test image session, each of which consisted of 24 and 35 runs, respectively. Each run contained 55 stimulus blocks consisting of 50 blocks with different images and five randomly interspersed repetition blocks where the same image as in the previous block was presented. In each stimulus block an image ( $12 \times 12$  degree) was flashed at 2 Hz for 9 seconds. Images were presented on the center of the display with a central fixation spot. The color of the fixation spot changed from white to red for 0.5

seconds before each stimulus block began to indicate the onset of the block. Extra 33-second and 6-second rest periods were added to the beginning and end of each run, respectively. Subjects maintained steady fixation throughout each run, and performed a one-back repetition detection task on the images, responding with a button press for each repetition to maintain their attention on the presented images. In the training image session, a total of 1,200 images from 150 different object categories (eight images from each category) were each presented only once. In the test image session, a total of 50 images from 50 object categories (one image from each category) were presented 35 times each. Note that the categories in the test image session were not used in the training image session. The presentation order of the categories was randomized across runs.

In the imagery experiment, the subjects were required to visually imagine images from one of the 50 object categories that were presented in the test image session of the image presentation experiment. Prior to the experiment, 50 visual image exemplars from each category were exposed to train the correspondence between object names and the visual images specified by the names. The imagery experiment consisted of 20 runs and each run contained 25 imagery blocks. Each imagery block consisted of a three second cue period, a 15-second imagery period, a 3-second evaluation period, and a 3-second rest period. Extra 33-second and 6-second rest periods were added to the beginning and the end of each run, respectively. During the rest periods, a white fixation spot was presented at the center of the display. The color of the fixation spot changed from white to red for 0.5 seconds to indicate the onset of the blocks from 0.8 seconds before each cue period began. During the cue period, words describing the names of the 50 categories presented in the test image session of the image presentation experiment were visually presented around the center of the display (one target and 49 distractors). The position of each word was randomly changed across blocks to avoid contamination of cue-specific effects on the fMRI response during imagery periods. The word of the category to be imagined was presented with a red color (target) and the other words were presented in black (distractors). The onset and the end of the imagery periods were signaled by beep sounds. The



subjects were required to start imagining as many object images pertaining to the category described by the red word as possible. Their eyes were closed from the first beep sound to the second beep sound. After the second beep sound, the word of the target category was presented at the center of the display to allow the subjects evaluate the vividness of their mental imagery on a five-point scale (very vivid, fairly vivid, rather vivid, not vivid, cannot recognize the target) by a button press. The 25 categories in each run were pseudo-randomly selected from 50 categories such that the two consecutive runs contained all the 50 categories.

### **Retinotopy experiment**

The retinotopy experiment followed the conventional protocol<sup>42,43</sup> using a rotating wedge and an expanding ring of a flickering checkerboard. The data were used to delineate the borders between each visual cortical area, and to identify the retinotopic map (V1–V4) on the flattened cortical surfaces of individual subjects.

### **Localizer experiment**

We performed functional localizer experiments to identify the lateral occipital complex (LOC), fusiform face area (FFA), and parahippocampal place area (PPA) for each individual subject<sup>44-46</sup>. The localizer experiment consisted of four to eight runs and each run contained 16 stimulus blocks. In this experiment, intact or scrambled images ( $12 \times 12$  degree) of face, object, house, and scene categories were presented at the center of the screen. Each of eight stimulus types (four categories  $\times$  two conditions) was presented twice per run. Each stimulus block consisted of a 15-second intact or scrambled stimulus presentation. The intact and scrambled stimulus blocks were presented successively (the order of the intact and scrambled stimulus blocks was random), followed by a 15-second rest period consisting of a uniform gray background. Extra 33-second and 6-second rest periods were added to the beginning and end of each run, respectively. In each stimulus block, 20 different images of the same type were presented for 0.3 seconds, followed by intervening

0.4-second-long blanks.

### **MRI acquisition**

fMRI data were collected using 3.0-Tesla scanner located at the ATR Brain Activity Imaging Center. An interleaved T2\*-weighted gradient-EPI scan was performed to acquire functional images to covering the entire brain (image presentation, imagery, and localizer experiments: TR, 3,000 ms; TE, 30 ms; flip angle, 80 deg; FOV,  $192 \times 192$  mm; voxel size,  $3 \times 3 \times 3$  mm; slice gap, 0 mm; number of slices, 50) or the entire occipital lobe (retinotopy experiments; TR, 2,000 ms; TE, 30 ms; flip angle, 80 deg; FOV,  $192 \times 192$  mm; voxel size,  $3 \times 3 \times 3$  mm; slice gap, 0 mm; number of slices, 30). T2-weighted turbo spin echo images were scanned to acquire high-resolution anatomical images of the same slices used for the EPI (image presentation, imagery, and localizer experiments: TR, 7,020 ms; TE, 69 ms; flip angle, 160 deg; FOV,  $192 \times 192$  mm; voxel size,  $0.75 \times 0.75 \times 3.0$  mm; retinotopy experiments: TR, 6,000 ms; TE, 57 ms; flip angle, 160 deg; FOV,  $192 \times 192$  mm; voxel size,  $0.75 \times 0.75 \times 3.0$  mm). T1-weighted magnetization-prepared rapid acquisition gradient-echo (MP-RAGE) fine-structural images of the entire head were also acquired (TR, 2,250 ms; TE, 3.06 ms; TI, 900 ms; flip angle, 9 deg, FOV,  $256 \times 256$  mm; voxel size,  $1.0 \times 1.0 \times 1.0$  mm).

### **MRI data preprocessing**

The first 9-second scans for experiments with TR = 3 seconds (image presentation, imagery, and localizer experiments) and 8-second scans for experiments with TR = 2 seconds (retinotopy experiments) of each run were discarded to avoid MRI scanner instability. The acquired fMRI data underwent three-dimensional motion correction by SPM5 (<http://www.fil.ion.ucl.ac.uk/spm>). The data were then coregistered to the within-session high-resolution anatomical image of the same slices used for EPI and subsequently to the whole-head high-resolution anatomical image. The coregistered data were then reinterpolated by  $3 \times 3 \times 3$  mm voxels.

For the data from the image presentation experiment and the imagery experiment, after within-run linear trend removal, voxel amplitudes were normalized relative to the mean amplitude of the entire time course within each run. The normalized voxel amplitudes from each of the two experiments were then averaged within each 9-second stimulus block (three volumes; image presentation experiment) or within each 15-second imagery period (five volumes; imagery experiment) respectively after shifting the data by 3 seconds (one volume) to compensate for hemodynamic delays.

### **Region of interest (ROI) selection**

V1, V2, V3, and V4 were delineated by the standard retinotopy experiment<sup>42,43</sup>. The lateral occipital complex (LOC), the fusiform face area (FFA), and the parahippocampal place area (PPA) were identified using conventional functional localizers<sup>44,46</sup>. The retinotopy experiment data were transformed to Talairach coordinates and the visual cortical borders were delineated on the flattened cortical surfaces using BrainVoyager QX (<http://www.brainvoyager.com>). The voxel coordinates around the gray-white matter boundary in V1–V4 were identified and transformed back into the original coordinates of the EPI images. The localizer experiment data were analyzed using SPM5. The voxels showing significantly higher activation in response to objects, faces, or scenes than for scrambled images ( $t$  test, uncorrected  $p < 0.05$  or  $0.01$ ) were identified, and defined as LOC, FFA, and PPA, respectively. A continuous region covering LOC, FFA, and PPA was manually delineated on the flattened cortical surfaces, and the region was defined as the *higher visual cortex* (HVC). Voxels overlapping with V1–V3 were excluded from HVC. Voxels from V1–V4 and HVC were combined to define the *visual cortex* (VC). In the regression analysis, voxels showing the highest correlation coefficient with the target variable in the model training session were selected to predict each feature (at most 500 voxels for V1, V2, V3, V4, LOC, FFA, and PPA; 1,000 voxels for VC).

## **Visual features**

We used four types of computational models: a convolutional neural network (CNN)<sup>17</sup>, the HMAX model<sup>19</sup>, GIST descriptor<sup>21</sup>, and the scale invariant feature transform (SIFT)<sup>15</sup> combined with “Bag of Features (BoF)”<sup>16</sup> to construct visual features from images. The features with a model-training phase (HMAX and SIFT+BoF) used 1,000 images belonging to the categories used in the model training session (150 categories) for model training. Each model is further described in the following subsections.

### ***Convolutional neural network (CNN)***

We computed visual features from the images using the CNN model proposed in a previous study<sup>17</sup>. We used the *Caffe* implementation of CNN, which was trained with images in *ImageNet*<sup>30</sup> to classify 1,000 object categories. The CNN consisted of five convolutional layers and three subsequent fully-connected layers. We randomly selected 1,000 units in each of the first to seventh layers and used all 1,000 units in the eighth layer. We represented each image by a vector of those units’ outputs, and named them as the CNN1–CNN8 model, respectively. Because we used the pre-trained CNN model, those 1,000 categories included the categories used in the test image session and the imagery experiment (20 categories were overlapped). However, the identification performance for the categories that did not belong to the CNN-training categories (30 non-overlapping categories) was qualitatively similar to the main results (Fig. 8 and Supplementary Fig. 9).

### ***HMAX***

In the HMAX model<sup>18,20</sup>, features are computed hierarchically in multiple layers. These layers consist of an image layer and six subsequent layers (S1, C1, S2, C2, S3, and C3), which are built from the previous ones by alternating template matching and max operations. In the calculations at each layer, we employed the same parameters as in a previous study<sup>19</sup>, except that the number of features in layer C2 and C3 was set to 1,000. We represented each image by a vector of the three types of HMAX

features, which consisted of 1,000 randomly selected outputs of units in layers S1, S2 and C2, and all 1,000 outputs in layer C3. We defined these outputs as HMAX1, HMAX2, and HMAX3 features in the analyses.

### ***GIST***

To compute GIST, an image was first converted to gray-scale and resized to have a maximum width of 256 pixels. Next, the image was filtered using a set of Gabor filters (16 orientations, four scales). After that, the filtered images were segmented by a four by four grid (16 blocks), and then the filtered outputs within each block were averaged to extract 16 responses for each filter. The responses from multiple filters were concatenated to create a 1,024 dimensional feature vector for each image ( $16 [\text{orientations}] \times 4 [\text{scales}] \times 16 [\text{blocks}] = 1,024$ ).

### ***SIFT with BoF (SIFT+BoF)***

The visual features using the SIFT with BoF approach were calculated from SIFT descriptors. We computed SIFT descriptors from the images using the VLFeat<sup>47</sup> (<http://www.vlfeat.org>) implementation of dense SIFT. In the BoF approach, each component of the visual feature vector (visualwords) is created by vector-quantizing extracted descriptors. Using about one million SIFT descriptors calculated from an independent training image set, we performed k-means clustering to create a set of 1,000 visualwords. The SIFT descriptors extracted from each image were quantized into visualwords using the nearest cluster center, and the frequency of each visualword was calculated to create a BoF histogram for each image. Finally, all of the histograms obtained through the above processing underwent  $L_1$  normalization to become unit norm vectors.

### **Visual feature decoding**

We constructed a model to predict the visual feature vectors of seen objects from fMRI activity using a linear regression function. Here, we used sparse linear regression (SLR;

[http://www.cns.atr.jp/cbi/sparse\\_estimation/index.html](http://www.cns.atr.jp/cbi/sparse_estimation/index.html))<sup>31</sup> that can automatically select the important features for prediction. The sparse estimation is known to perform well when the dimensionality of the explanatory variable is high, as is the case with fMRI data<sup>51</sup>.

Given an fMRI sample  $\mathbf{x} = \{x, \dots, x_d\}^T$  consisting of the activities of  $d$  voxels' as input, the regression function can be expressed by

$$y(\mathbf{x}) = \sum_{i=1}^d w_i x_i + w_0,$$

where  $x_i$  is a scalar value specifying the fMRI amplitude of the voxel  $i$ ,  $w_i$  is the weight of voxel  $i$ , and  $w_0$  is the bias. For simplicity, the bias  $w_0$  is absorbed into the weight vector such that  $\mathbf{w} = \{w_0, \dots, w_d\}^T$ . The dummy variable  $x_0 = 1$  is introduced into the data such that  $\mathbf{x} = \{x_0, \dots, x_d\}^T$ . Using this function, we modeled the  $l$ th component of each visual feature vector as a target variable  $t_l$  ( $l \in \{1, \dots, L\}$ ) that is explained by the regression function  $y(\mathbf{x})$  with additive Gaussian noise as described by

$$t_l = y(\mathbf{x}) + \epsilon$$

where  $\epsilon$  is a zero mean Gaussian random variable with noise precision  $\beta$ .

Given a training data set, SLR computes the weights and bias for the regression function such that the regression function optimizes an objective function. To construct the objective function, we first express the likelihood function by

$$P(\mathbf{t}_l | \mathbf{X}, \mathbf{w}, \beta) = \prod_{n=1}^N \frac{1}{(2\pi)^{1/2}} \beta^{1/2} \exp \left\{ -\frac{1}{2} \beta (t_{ln} - \mathbf{w}^T \mathbf{x}_n)^2 \right\},$$

where  $N$  is the number of samples,  $\mathbf{X}$  is an  $N \times (d + 1)$  fMRI data matrix whose  $n^{\text{th}}$  row is the  $d + 1$ -dimensional vector  $\mathbf{x}_n$ , and  $\mathbf{t}_l = \{t_{l1}, \dots, t_{ln}\}^T$  are the samples of a component of the visual feature vector.

We performed Bayesian parameter estimation, and adopted the automatic relevance determination (ARD) prior<sup>31</sup> to introduce sparsity into the weight estimation. We considered the estimation of the weight parameter  $\mathbf{w}$  given the training data sets  $\{\mathbf{X}, \mathbf{t}_l\}$ . We assumed a Gaussian distribution prior for the weights  $\mathbf{w}$  and non-informative priors for the weight precision parameters  $\boldsymbol{\alpha} = \{\alpha_0, \dots, \alpha_d\}^T$  and the noise precision parameter  $\beta$ , which are described as

$$P_0(\mathbf{w}|\boldsymbol{\alpha}) = \prod_{i=0}^d \frac{1}{(2\pi)^{1/2}} \alpha_i^{1/2} \exp\left\{-\frac{1}{2} \alpha_i w_i^2\right\},$$

$$P_0(\boldsymbol{\alpha}) = \prod_{i=0}^d \frac{1}{\alpha_i},$$

$$P_0\left(\frac{1}{\beta}\right) = \frac{1}{\beta}.$$

In the Bayesian framework, we consider the joint probability distribution of all the estimated parameters, and the weights can be estimated by evaluating the following joint posterior probability of  $\mathbf{w}$ :

$$P(\mathbf{w}, \boldsymbol{\alpha}, \beta | \mathbf{X}, \mathbf{t}_l) = \frac{P(\mathbf{t}_l, \mathbf{w}, \boldsymbol{\alpha}, \beta | \mathbf{X})}{\int d\mathbf{w} d\boldsymbol{\alpha} d\beta P(\mathbf{t}_l, \mathbf{w}, \boldsymbol{\alpha}, \beta | \mathbf{X})} = \frac{P(\mathbf{t}_l | \mathbf{X}, \mathbf{w}, \beta) P_0(\mathbf{w} | \boldsymbol{\alpha}) P_0(\boldsymbol{\alpha}) P_0(\beta)}{\int d\mathbf{w} d\boldsymbol{\alpha} d\beta P(\mathbf{t}_l, \mathbf{w}, \boldsymbol{\alpha}, \beta | \mathbf{X})}.$$

Given that the evaluation of the joint posterior probability  $P(\mathbf{w}, \boldsymbol{\alpha}, \beta | \mathbf{X}, \mathbf{t}_l)$  is analytically intractable, we approximate it using the variational Bayesian (VB) method<sup>31,49</sup>. See Sato (2001)<sup>50</sup>, Sato et al. (2004)<sup>51</sup>, and Ting et al. (2005, 2008)<sup>52,53</sup> for details on the parameter estimation algorithm. The results obtained using the standard linear regression model with maximum likelihood estimation were qualitatively similar to those obtained using our Bayesian sparse linear regression model.

We trained a linear regression model that predicts a feature vector of individual visual features for

seen object categories given fMRI samples in the training image session. For test datasets, fMRI samples corresponding to the same categories (35 samples in the test image session, 10 samples in the imagery experiment) were averaged across trials to increase the signal to noise ratio of the fMRI signals. Using the learned models, we predicted feature vectors of seen/imagined objects from averaged fMRI samples to construct one predicted feature vector for each category in the image presentation experiment and the imagery experiment.

### **Identification analysis**

In the identification analyses, categories of seen/imagined objects were identified using the visual feature vectors decoded from fMRI activity patterns. Prior to the identification analysis, visual feature vectors were computed for all of the preprocessed images (see Methods, Visual images) in all of the categories (15,372 categories) except for those used in the fMRI experiments and their hypernym/hyponym categories and those used for visual feature model training (HMAX and SIFT+BoF). The visual feature vectors of individual images were averaged within each category to create object feature vectors for all of the categories to form the candidate category set. Then, using the trained SLR models, we predicted the visual feature vectors of the seen/imagined objects from fMRI samples. We computed the Pearson's correlation coefficients between the decoded feature vectors and the feature vectors of each category in the candidate sets. To quantify the performance for a variable number of candidates, we created candidate sets consisting of the seen/imagined categories and randomly selected categories. None of the categories in the candidate set were used for the training of the decoding model. Given a decoded feature vector, category identification was conducted by selecting the category with the highest correlation coefficient among the candidate sets.



## References

1. Haxby, J.V. et al. Distributed and overlapping representations of faces and object in ventral temporal cortex. *Science* **293**, 2425–2430 (2001).
2. Kamitani, Y. & Tong, F. Decoding the visual and subjective contents of the human brain. *Nat. Neurosci.* **8**, 679–685 (2005).
3. Harrison, S.A. & Tong, F. Decoding reveals the contents of visual working memory in early visual areas. *Nature* **458**, 632–635 (2009).
4. Albers, A.M., Kok, P., Toni, I., Dijkerman, H.C. & De Lange, F.P. Shared representations for working memory and mental imagery in early visual cortex. *Curr. Biol.* **23**, 1–5 (2013).
5. Xing, Y., Ledgeway, T., McGraw, P.V. & Schluppeck, D. Decoding working memory of stimulus contrast in early visual cortex. *J. Neurosci.* **33**, 10301–10311 (2013).
6. Reddy, L., Tsuchiya, N. & Serre, T. Reading the mind's eye: Decoding category information during mental imagery. *Neuroimage* **50**, 818–825 (2010).
7. Cichy, R.M., Heinzle, J. & Haynes, J.D. Imagery and perception share cortical representations of content and location. *Cereb. Cortex* **22**, 372–380 (2011).
8. Stokes, M., Thompson, R., Cusack, R. & Duncan, J. Top-down activation of shape-specific population codes in visual cortex during mental imagery. *J. Neurosci.* **29**, 1565–1572 (2009).
9. Johnson, M.R. & Johnson, M.K. Decoding individual natural scene representations during perception and imagery. *Front. Hum. Neurosci.* **8**, (2014).
10. Horikawa, T., Tamaki, M., Miyawaki, Y. & Kamitani, Y. Neural decoding of visual imagery during sleep. *Science* **340**, 639–642 (2013).
11. Kay, K.N., Naselaris, T., Prenger, R.J. & Gallant, J.L. Identifying natural images from human brain activity. *Nature* **452**, 352–355 (2008).
12. Naselaris, T., Prenger, R.J., Kay, K.N., Oliver, M. & Gallant, J.L. Bayesian

- reconstruction of natural images from human brain activity. *Neuron* **63**, 902–915 (2009).
13. Miyawaki, Y. et al. Visual image reconstruction from human brain activity using a combination of multiscale local image decoders. *Neuron* **60**, 915–929 (2008).
  14. Naselaris, T., Olman, C.A., Stansbury, D.E., Ugurbil, K. & Gallant, J.L. A voxel-wise encoding model for early visual areas decodes mental images of remembered scenes. *Neuroimage* **105**, 215–228 (2015).
  15. Lowe, D.G. Object recognition from local scale-invariant features, *Proc. IEEE International Conference on Computer Vision* 1150–1157 (1999).
  16. Csurka, G., Dance, C., Fan, L., Willarnowski, J. & Bray, C. Visual categorization with bags of keypoints. *ECCV* **1**, 1–2 (2004).
  17. Krizhevsky, A., Sutskever, I. & Hinton, G. ImageNet classification with deep convolutional neural networks. *NIPS* (2012).
  18. Riesenhuber, M. & Poggio, T. Hierarchical models of object recognition in cortex. *Nat. Neurosci.* **2**, 1019–1025 (1999).
  19. Serre, T., Wolf, L., Bileschi, S., Riesenhuber, M. & Poggio, T. Robust object recognition with cortex-like mechanisms. *IEEE Trans. Pattern Anal. Mach. Intell.* **29**, 411–426 (2007).
  20. Mutch, J. & Lowe, D.G. Object class recognition and localization using sparse features with limited receptive fields. *IJCV* **80**, 45–57 (2008).
  21. Oliva, A. & Torralba, A. Modeling the shape of the scene: A holistic representation of the spatial envelope. *International journal of computer vision* **42**, 145–175 (2001).
  22. Cadieu, C.F. et al. Deep neural networks rival the representation of primate IT cortex for core visual object recognition. *PLoS Comput. Biol.* **10**: e1003963 (2014).
  23. Yamins, D.L.K. et al. Performance-optimized hierarchical models predict neural responses in higher visual cortex. *Proc. Natl. Acad. Sci. U S A.* **111**, 8619–8624

- (2014).
24. Khaligh-Razavi, S.M. & Kriegeskorte, N. Deep supervised, but not unsupervised, models may explain IT cortical representation. *PLoS Comput. Biol.* **10** (2014).
  25. Güçlü, U. & van Gerven M.A.J Deep neural networks reveal a gradient in the complexity of neural representations across the ventral stream. *J. Neurosci.* **35**, 100005–100014 (2015).
  26. Rice, G.E., Watson, D.M., Hartley, T. & Andrews, T.J. Low-level image properties of visual objects predict patterns of neural response across category-selective regions of the ventral visual pathway. *J. Neurosci.* **34**, 8837–8844 (2014).
  27. Leeds, D.D., Seibert, D.A., Pyles, J.A. & Tarr, M.J. Comparing visual representations across human fMRI and computational vision. *J. Vis.* **13** (2013)
  28. J. Deng et al. Imagenet: A large-scale hierarchical image database. *IEEE CVPR* (2009).
  29. Hubel, D. & Wiesel, T. Receptive fields, binocular interaction and functional architecture in the cat's visual cortex. *J. Physiol.* **160**, 106–154 (1962).
  30. Hubel, D. & Wiesel, T. Receptive fields and functional architecture in two nonstriate visual areas (18 and 19) of the cat. *J. Neurophysiol.* **28**, 229–289 (1965).
  31. Bishop, C.M. *Pattern Recognition and Machine Learning*. New York: Springer (2006).
  32. Fellbaum, C. *WordNet: An Electronic Lexical Database*. Cambridge, MA: MIT Press (1998).
  33. Pylyshyn, Z.W. Mental imagery: in search of a theory. *Behav. Brain Sci.* **25**, 157–237 (2002).
  34. Pearson, J. & Kosslyn, S.M. The heterogeneity of mental representation: Ending the imagery debate. *Proc. Natl. Acad. Sci. U S A*. doi: 10.1073/pnas.1504933112 (2015).
  35. Ullman, S., Vidal-Naquet, M. & Sali, E. Visual features of intermediate complexity

- and their use in classification. *Nat. Neurosci.* **5**, 682–687 (2002).
36. Fujita, I., Tanaka, K., Ito, M. & Cheng, K. Columns for visual features of objects in monkey inferotemporal cortex. *Nature* **360**, 343–346 (1992).
  37. Kobatake, E. & Tanaka, K. Neuronal selectivities to complex object features in the ventral visual pathway of the macaque cerebral cortex. *J. Neurophysiol.* **71**, 856–867 (1994).
  38. Kriegeskorte, N., Mur, M. & Bandettini, P. Representational similarity analysis – connecting the branches of systems neuroscience. *Front. Syst. Neurosci.* **2** (2008).
  39. Kriegeskorte, N. Relating population-code representations between man, monkey, and computational models. *Front. Neurosci.* **3**, 363–373 (2009).
  40. Kriegeskorte, N. & Kievit, R.A. Representational geometry: integrating cognition, computation, and the brain. *Trends in Cognitive Sciences* **17**, 401–412 (2013).
  41. Nili, H. et al. A Toolbox for Representational Similarity Analysis. *PLoS Comput. Biol.* **10** (2014).
  42. Engel, S.A. et al. fMRI of human visual cortex. *Nature* **369**, 525 (1994).
  43. Sereno, M.I. et al. Borders of multiple visual areas in humans revealed by functional magnetic resonance imaging. *Science* **268**, 889–893 (1995).
  44. Kourtzi, Z., Kanwisher, N. Cortical regions involved in perceiving object shape. *J. Neurosci.* **20**, 3310–3318 (2000).
  45. Kanwisher, N., McDermott, J. & Chun, M.M. The fusiform face area: a module in human extrastriate cortex specialized for face perception. *J. Neurosci.* **17**, 4302–4311 (1997).
  46. Epstein, R. & Kanwisher, N. A cortical representation of the local visual environment. *Nature* **392**, 598–601 (1998).
  47. Vedaldi, A. & Fulkerson, B. VLFeat: An open and portable library of computer vision algorithms. (version 0.9.9) (2008).

48. Yamashita, O., Sato, M.A., Yoshioka, T., Tong, F. & Kamitani, Y. Sparse estimation automatically selects voxels relevant for the decoding of fMRI activity patterns. *Neuroimage* **42**, 1414–1429 (2008).
49. Attias, H. Inferring parameters and structure of latent variable models by variational Bayes. *Proceedings of 15th Conference on Uncertainty in Artificial Intelligence* 21–30 (1999).
50. Sato, M.A. Online model selection based on the variational Bayes. *Neural Comp.* **13**, 1649–1681 (2001).
51. Sato, M.A. et al. Hierarchical Bayesian estimation for MEG inverse problem. *Neuroimage* **23**, 806–826 (2004).
52. Ting, J.A. et al. Predicting EMG data from M1 neurons with Variational Bayesian least squares. *NIPS* (2005).
53. Ting, J.A. et al. Variational Bayesian least squares: an application to brain machine interface data. *Neural Networks* **21**, 1112–1131 (2008).

## Acknowledgements

The authors thank Yoichi Miyawaki, Yasuhito Sawahata, Makoto Takemiya, and Kei Majima for helpful comments on the manuscript; and Mitsuaki Tsukamoto for help with data collection. This research was supported by grants from JSPS KAKENHI Grant number 26119536, 26870935, 15H05920, 15H05710, a contract with the Ministry of Internal Affairs and Communications entitled “Novel and innovative R&D making use of brain structures”, ImPACT Program of Council for Science, Technology and Innovation (Cabinet Office, Government of Japan), and the New Energy and Industrial Technology Development Organization (NEDO).

## Author contributions

TH and YK designed the study. TH performed experiments and analyses. TH and YK wrote the

paper.

## Competing financial interests

The authors declare that they have no competing financial interests.

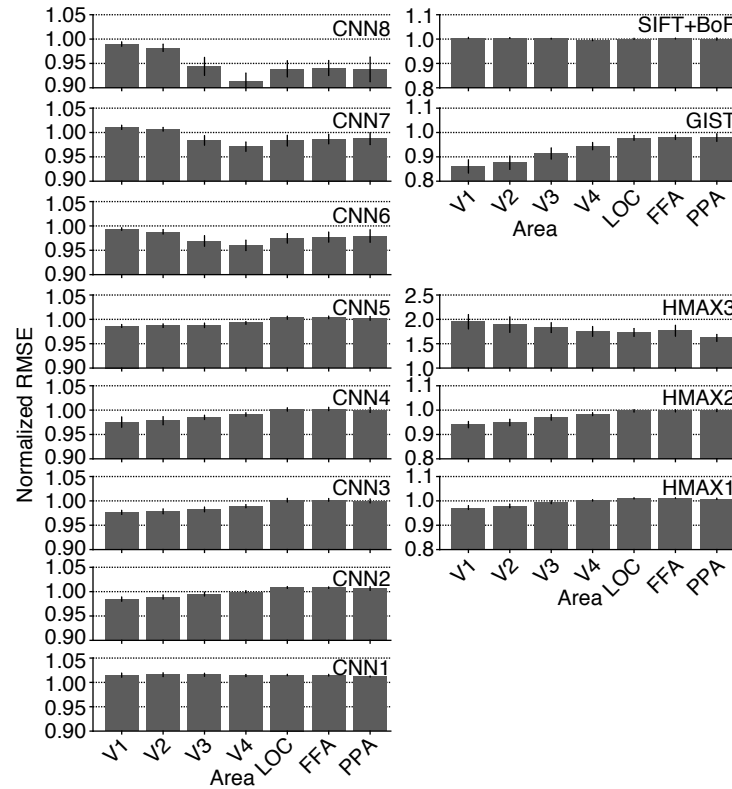
# **Supplementary Information for Generic Decoding of Seen and Imagined Objects using Hierarchical Visual Features**

Table of contents

## **1 Supplementary figures**

1. Image feature prediction accuracy from multiple brain areas evaluated by normalized root mean square error
2. Distributions of object feature decoding accuracy for seen and imagined conditions
3. Identification performance as a function of the number of average samples
4. Identification performance for all combinations of feature types/layers and brain areas
5. Identification performance obtained by image feature decoders
6. Identification performance for all combinations of feature types/layers and brain areas obtained by image feature decoders
7. Identification accuracy as a function of the number of feature units
8. Identification accuracy with true image feature values (generic object recognition, GOR)
9. Identification accuracy for object categories not used for CNN model training

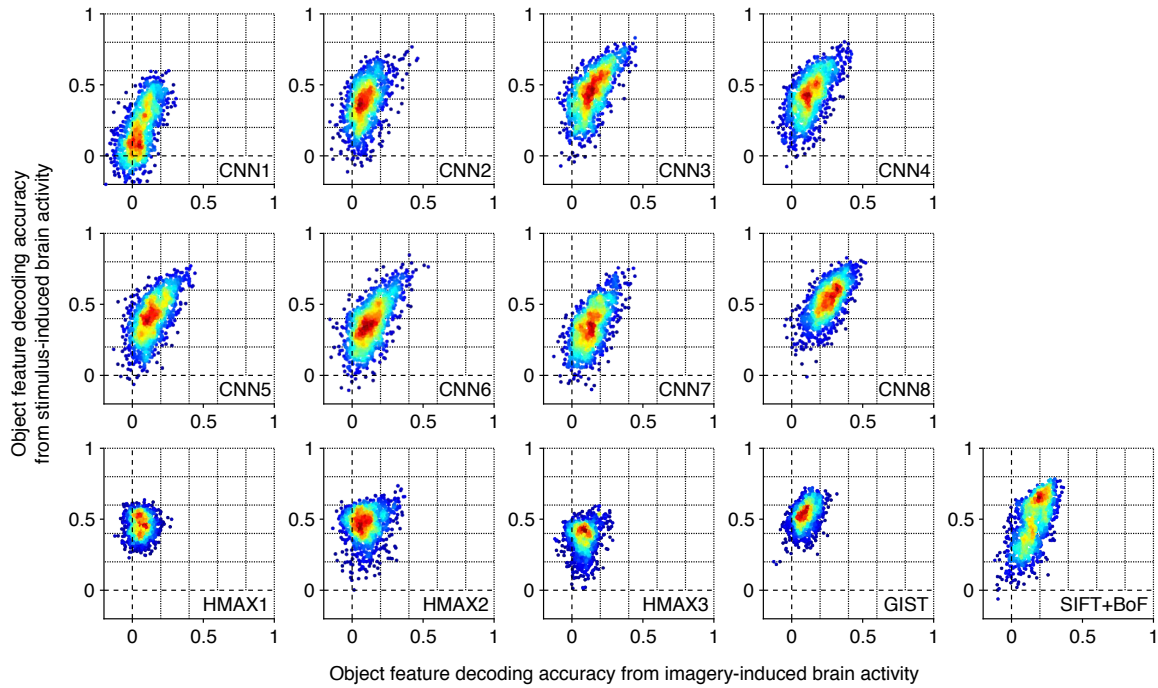
## Supplementary Figures



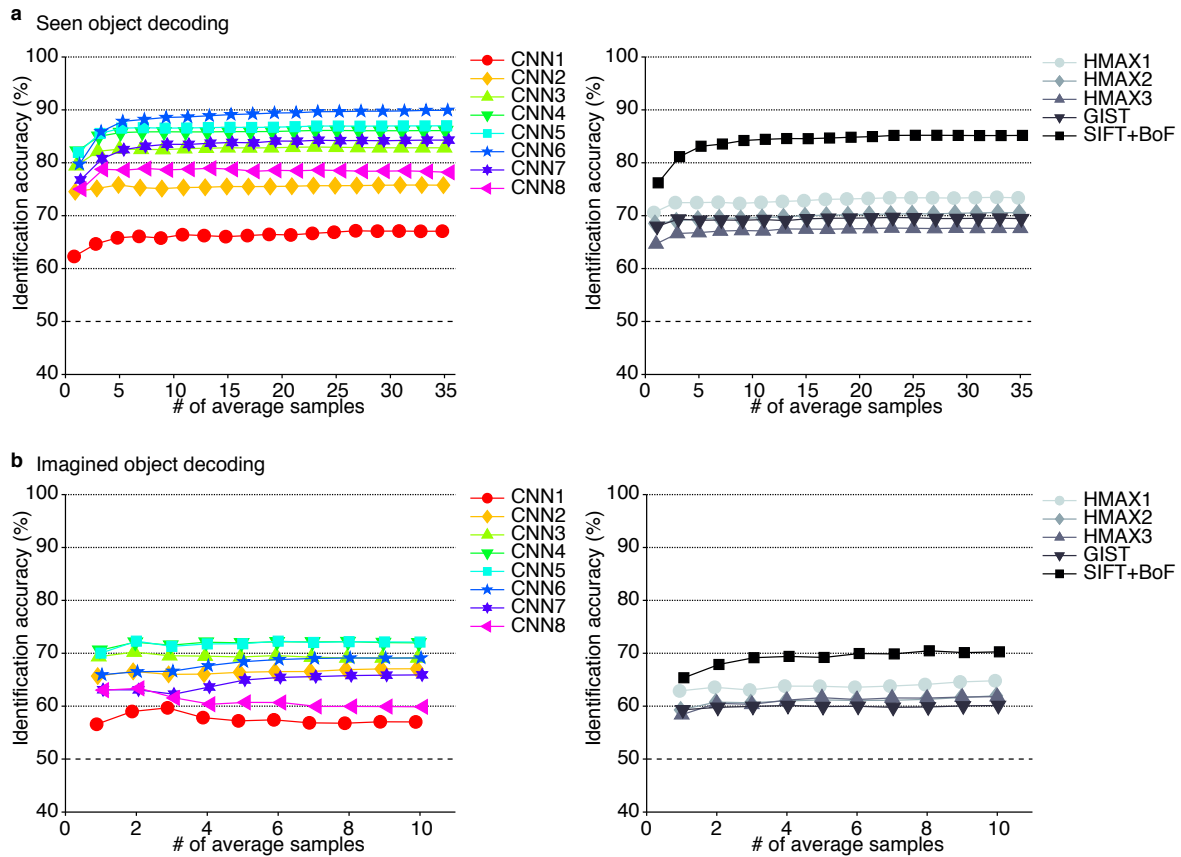
**Supplementary Figure 1 | Image feature prediction accuracy from multiple brain areas evaluated by normalized root mean square error.** For each feature unit, the root mean square error (RMSE) between true and predicted values were calculated over 50 target categories, and then normalized by the standard deviation of the true values. The normalized RMSE (nRMSE) was averaged for each feature type/layer and brain area (error bars, 95% CI across five subjects). The range of the horizontal axis was changed for each visual feature for visualization purposes. This analysis replicated a general trend observed in the results based on correlation coefficients (Fig. 3b), showing that the higher-order visual features tended to be better predicted from fMRI signals in higher rather than lower cortical areas, and that lower-order visual features tended to be better predicted from fMRI signals in lower rather than higher cortical areas. However, nRMSE showed a different pattern



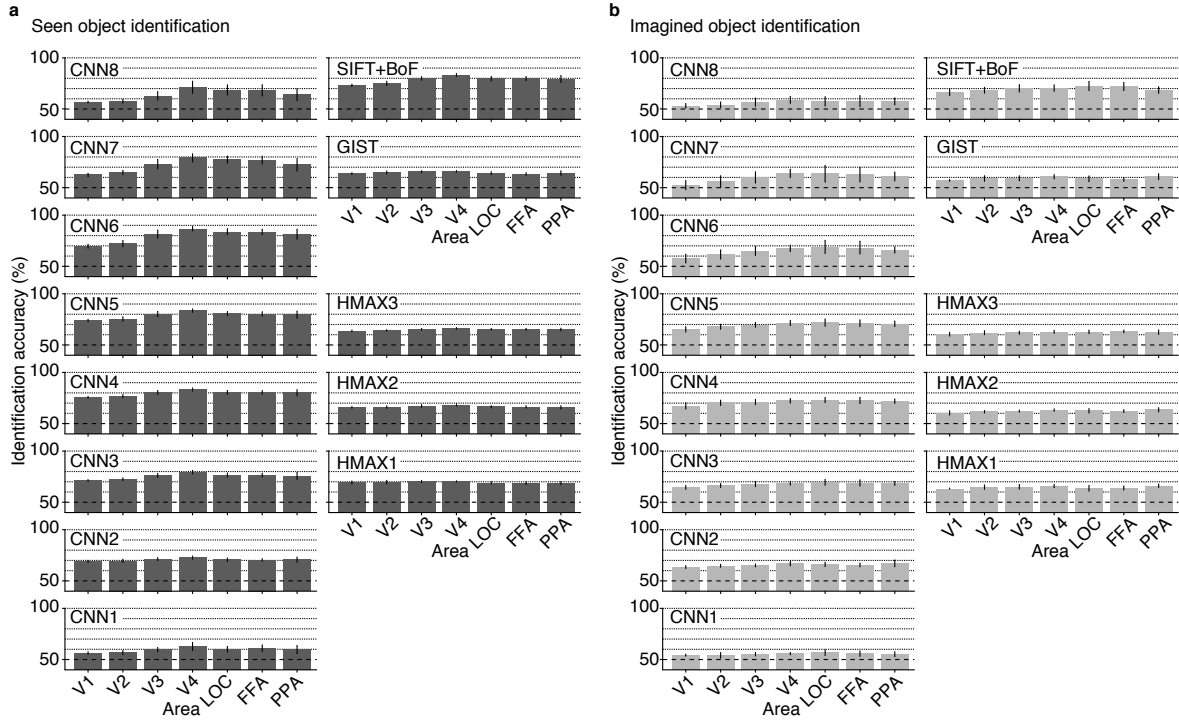
of performance from correlation when compared across feature types/layers. For example, HMAX3 showed the worst accuracy in nRMSE for all brain areas, while it attained a higher accuracy than several CNN features and SIFT+BoF in correlation.



**Supplementary Figure 2 | Distributions of object feature decoding accuracy for seen and imagined conditions.** Scatterplots of object feature decoding accuracy for the seen (vertical axis) and imagined (horizontal axis) conditions are shown for ~1,000 feature units. Each dot denotes the averaged feature decoding accuracy across five subjects (predicted from VC) for each feature unit. The color indicates the density of the dots. Although the mean accuracy spans from around 0.1 to 0.5 for the seen condition (Fig. 4a) and from 0.0 to 0.2 for the imagined condition (Fig. 4b), the accuracies of individual units are rather broadly distributed. A subset of units with high accuracies may substantially contribute to object decoding.

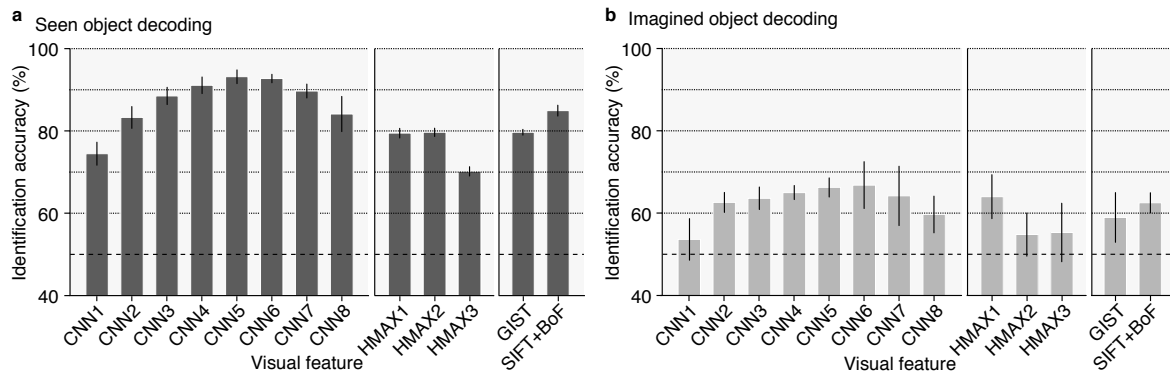


**Supplementary Figure 3 | Identification performance as a function of the number of average samples.** Identification accuracies as a function of the number of average samples are shown (identification from two categories; dashed line, chance level, 50%). **(a)** Seen object identification performance. The identification performance gradually improves with the number of average samples but saturates at fewer than ten samples. **(b)** Imagined object identification performance. Nearly equivalent performances are observed even without averaging multiple samples.

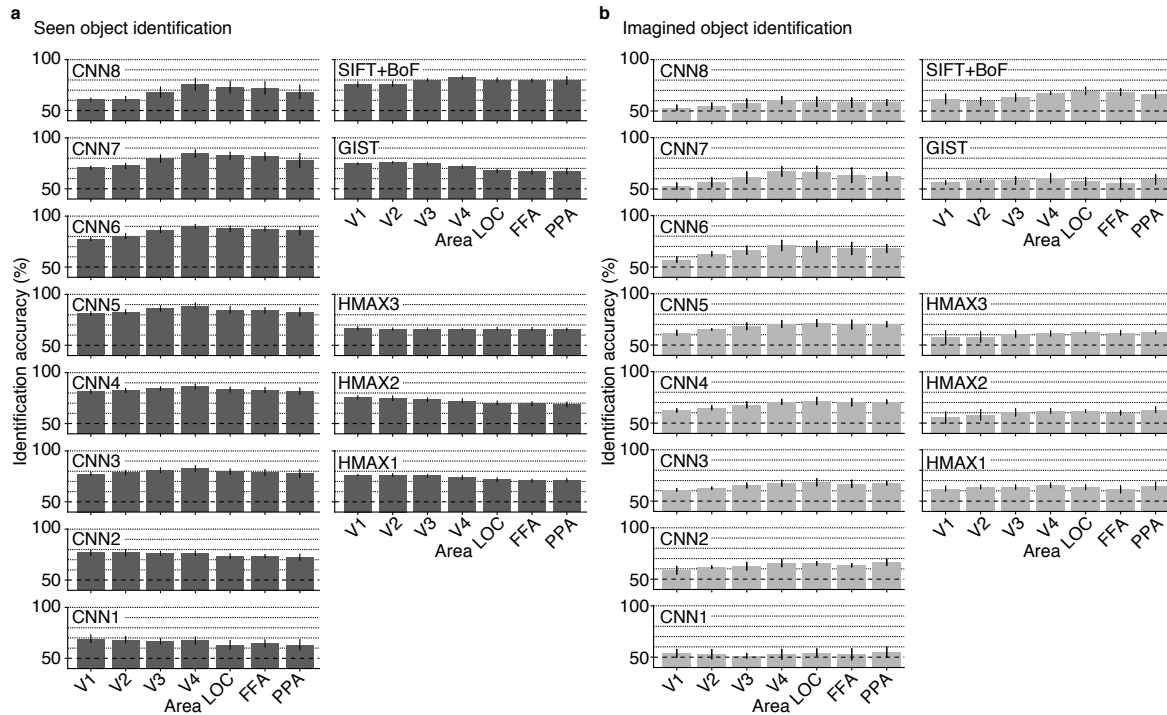


#### Supplementary Figure 4 | Identification performance for all combinations of feature

**types/layers and brain areas.** Identification was performed for all combinations of one of the 50 test object categories and one of the 15,322 candidate categories (identification from two categories; error bars, 95% CI across five subjects; dashed line, chance level, 50%). **(a)** Seen object identification performance. **(b)** Imagined object identification performance. Both seen and imagined objects were successfully identified at a statistically significant level with most of the feature–ROI combinations (91 and 90 out of a total of 91 feature–ROI pairs for seen and imagined conditions, respectively; *t* test, uncorrected  $p < 0.05$ ).

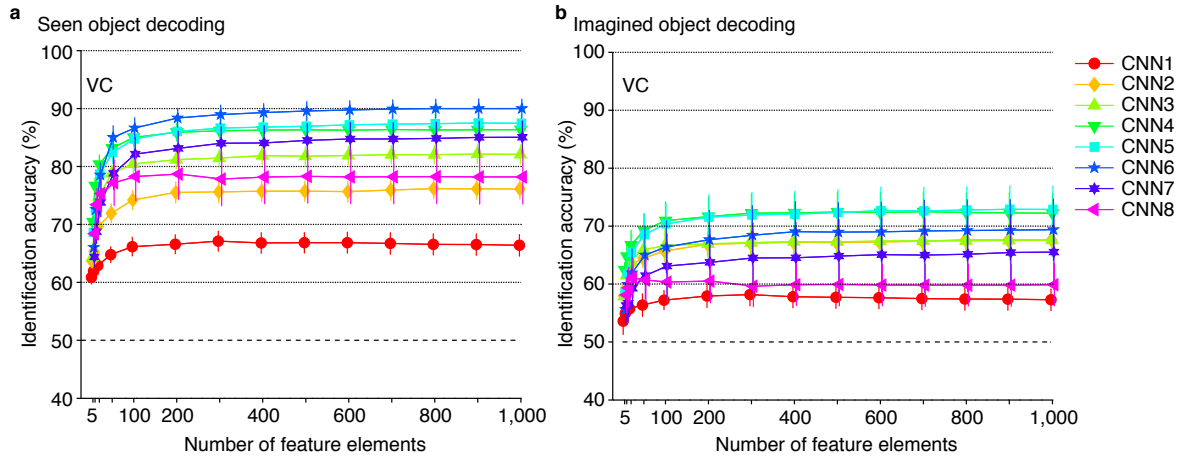


**Supplementary Figure 5 | Identification performance obtained by image feature decoders.** The same identification analysis as shown in Fig. 8 was performed with the decoders trained to predict image features of presented images (cf., Fig. 3; identification from two categories; error bars, 95% CI across five subjects; dashed line, chance level, 50%). **(a)** Seen object identification. **(b)** Imagined object identification. A similar pattern of performance across brain areas was observed as compared with Fig.8. The overall accuracy for seen object decoding tended to be higher with image feature decoders than with object feature decoders, while that for imagined object decoding tended to be lower with image feature decoders than with object feature decoders.



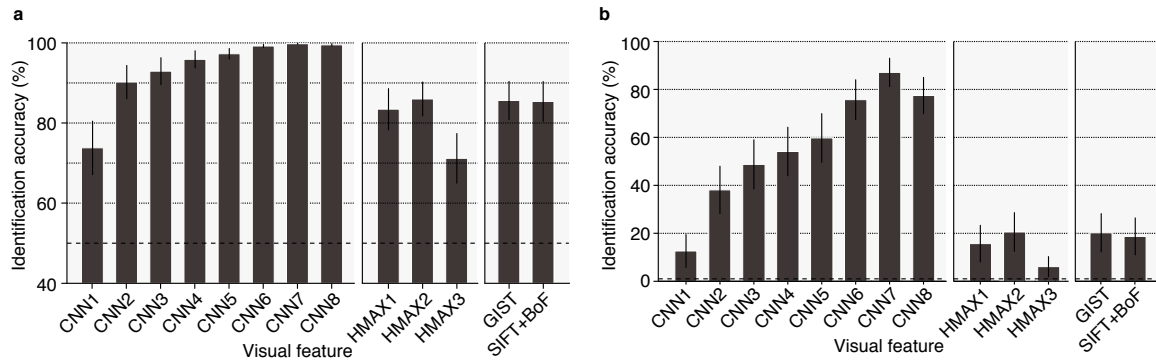
### Supplementary Figure 6 | Identification performance for all combinations of feature

**types/layers and brain areas obtained by image feature decoders.** The same identification analysis as shown in Supplementary Fig. 4 was performed with the decoders trained to predict image features of the presented images (cf., Fig. 3; identification from two categories; error bars, 95% CI across five subjects; dashed line, chance level, 50%). **(a)** Seen object identification. **(b)** Imagined object identification. Both seen and imagined objects were successfully identified with many feature–ROI combinations (91 and 84 out of a total of 91 feature–ROI pairs for seen and imagined conditions, respectively;  $t$  test, uncorrected  $p < 0.05$ ). In seen object identification, the performance for higher-order features tended to be better with higher visual areas, while that for lower-order features tended to be better with lower visual areas, as observed in the image feature prediction performance (Fig. 3). In imagined object identification, in contrast, all feature types/layers showed a similar trend of flat or slightly elevated accuracies in higher visual areas.



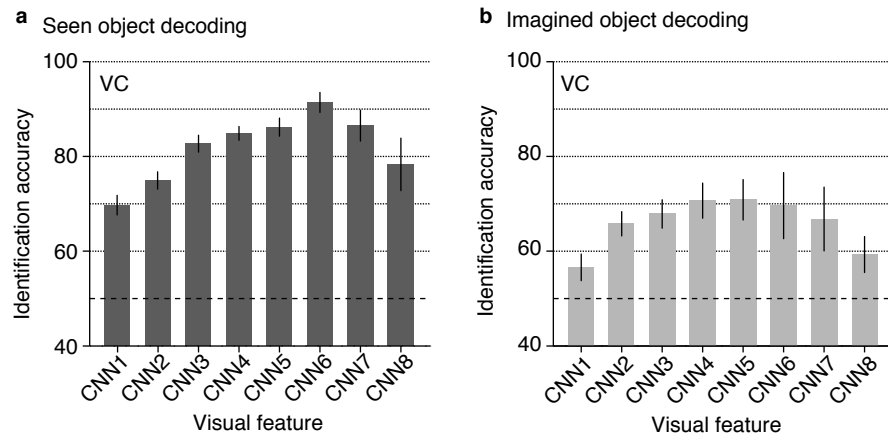
### Supplementary Figure 7 | Identification accuracy as a function of the number of feature units.

Identification was performed using a different number of feature units from CNN1–8 for all combinations of the 50 test object categories and 15,322 candidate categories (identification from two categories; predicted from VC). The analysis was repeated 10 times for each number of feature units, and the accuracy was pooled across 10 repetitions of category candidate selection and 50 test samples (error bars, 95% CI across five subjects; dashed lines, chance level, 50%). **(a)** Seen object identification. **(b)** Imagined object identification. The accuracies of most visual features were saturated at a few hundred units. The performance trend across feature types/layers remained nearly constant across the number of feature units, with the mid-level features showing highest accuracies.



**Supplementary Figure 8. Identification accuracy with true image feature values (generic object recognition, GOR).** The GOR identification performance for each visual feature is shown. The GOR performance is equivalent to the case when image features are perfectly predicted from brain activity using image feature decoders. **(a)** Identification from two categories. Identification was performed for all combinations of one of the 50 test object categories and one of the 15,322 candidate categories (error bars, 95% CI across 50 test categories; dashed line, chance level, 50%). **(b)** Identification from 100 categories. Identification was repeated for 100 candidate sets of randomly selected categories for each of the 50 test categories. The percentage of correct identifications was averaged across the candidate sets (error bars, 95% CI across 50 test categories; dashed line, chance level, 1%). The analysis showed a slightly poorer identification with CNN8 than with CNN7.





**Supplementary Figure 9 | Identification accuracy for object categories not used for CNN model training.** Mean identification accuracy for categories not used for CNN model training ( $n = 30$ ) were evaluated (identification from two categories; error bars, 95% CI across five subjects; dashed lines, chance level, 50%). These results were quantitatively similar to those of the main analysis (Fig. 8).